# Development of Free Surface Tracking Algorithms for Fusion Welding Simulations

Fang Wang
Department of Mechanical Engineering
University of Michigan, Ann Arbor, MI 48109, USA

William W. Schultz (Corresponding author)
Department of Mechanical Engineering
University of Michigan, Ann Arbor, Michigan 48109, USA
E-mail: schultz@umich.edu
Phone: 1-734-936-0351
Fax: 1-734-764-4256

Guo Xu
Department of Mechanical Engineering
University of Michigan, Ann Arbor, MI 48109, USA

S. Jack Hu
Department of Mechanical Engineering
University of Michigan, Ann Arbor, MI 48109, USA

Elijah Kannatey-Asibu, Jr.
Department of Mechanical Engineering
University of Michigan, Ann Arbor, MI 48109, USA

Wenkao Hou
Department of Mechanical Engineering
University of Michigan, Ann Arbor, MI 48109, USA

## Abstract

Most previous welding simulations are based on a flat weld pool surface and become unmeaningful when the surface deformation is significant. In recent years, some researchers have developed numerical models capable of simulating free surface motion in welding processes, but they focus on the discussions of physical equations, boundary conditions, and solutions, rather than the numerical algorithms. Engineers may find it difficult to reproduce these studies without considerable effort. In this paper, we develop an easy to follow numerical procedure for the simulation of fusion welding processes. Recommendations are made on the selection and implementation of numerical algorithms, while alternative methods are also reviewed. The simulation algorithms posed here are efficient and robust. They can simulate gas metal arc welding, gas tungsten arc welding, laser welding and plasma arc welding.

**Keywords**: Welding, Free Surface Tracking, Simulation, Numerical Methods

**Classification Numbers**: 65C20, 76M12, 62P30

## Nomenclature

| | |
|---|---|
| $\vec{B}$ | Magnetic field [Tesla] |
| $B_\theta$ | Circumferential magnetic field [Tesla] |
| $c$ | Specific heat [J/kg·K] |
| $D$ | Wire diameter [m] |
| $e$ | Internal energy [J/kg] |
| $f$ | Fractional fluid volume in a cell |
| $\vec{f}$ | Body force vector [N] |
| $F$ | Fractional fluid volume |
| $h$ | Enthalpy [J/kg] |
| $I$ | Current [A] |
| $\vec{J}$ | Current density vector [A/m$^2$] |
| $k$ | Thermal conductivity [W/m·K] |
| $n$ | Distance in normal direction [m] |
| $\vec{n}$ | Normal direction |
| $L$ | Latent heat [J/kg] |
| $p$ | Pressure [Pa] |
| $p^*$ | Pressure prediction [Pa] |
| $p'$ | Pressure correction [Pa] |
| $p_{arc}$ | Arc pressure [Pa] |
| $q$ | Heat flux [W/m$^2$] |
| $q'''$ | Heat generation rate [W/m$^3$] |
| $r$ | Radial coordinate [m] |
| $R_1$ | Principle radius of curvature in r-z plane [m] |
| $R_2$ | Principle radius of curvature in azimuthal direction [m] |

| | |
|---|---|
| Re | Reynolds Number |
| $s$ | Distance in tangential direction [m] |
| $\vec{s}$ | Direction vector of integration path |
| $t$ | Time [sec] |
| $T$ | Temperature [K] |
| $T_l$ | Liquidus temperature [K] |
| $T_m$ | Melting temperature [K] |
| $T_{room}$ | Room temperature [K] |
| $T_s$ | Solidus temperature [K] |
| $u$ | Velocity on the boundary of two cells [m/sec] |
| $u^*$ | Velocity prediction [m/sec] |
| $u'$ | Velocity correction [m/sec] |
| $\vec{v}$ | Velocity vector [m/sec] |
| $v_{feed}$ | Wire feed rate [m/sec] |
| $U$ | Welding voltage [V] |
| $V$ | Electric potential (voltage) [V] |
| $z$ | Axial coordinate [m] |
| $z'$ | Vertical distance to the arc root (starting point of current density) |
| $z'$ | Vertical distance to the starting point of heat input |
| $\vartheta$ | Artificial diffusion constant [ $Ohm \cdot m^3/\text{sec}$ ] |
| $\gamma$ | Surface tension coefficient [N/m] |
| $\delta f^+$ | Fluid flux from left cell to right cell |
| $\delta f^-$ | Fluid flux from right cell to left cell |
| $\delta h$ | Grid size of square cells [m] |
| $\delta_{ij}$ | Kronecker delta |
| $\delta t$ | Time increment in each computational step [sec] |
| $\eta$ | Arc efficiency |

$\eta_d$ Ratio of heat absorbed by the wire tip to the total absorbed by the metal

$\eta_p$ Ratio of heat absorbed by the weld pool to the total heat absorbed by metal

$\mu$ Dynamic viscosity [kg/m·sec]

$\mu_0$ Permeability of free space [$1.256637\times10^{-6}\ H/m$]

$\nu$ Kinematic viscosity [$m^2$/sec]

$\rho$ Density [$kg/m^3$]

$\tau_{ij}$ Stress tensor [Pa]

$\tau_{drag}$ Gas drag stress [Pa]

$\sigma$ Electrical conductivity [1/Ω·m]

$\sigma_j$ Distribution radius of current density [m]

$\sigma_q$ Distribution radius of heat flux [m]

Subscripts

| | |
|---|---|
| $nb$ | Neighboring cells |
| $n, s, w, e$ | The north, south, west and east faces of a cell |
| $N, S, W, E$ | The centers of the north, south, west and east neighboring cells |
| $P$ | The center of a cell |
| $l$, $s$ | Liquid, solid |
| $r$, $z$ | Radial and axial components |

## 1. Introduction

Fusion welding is a complex physicochemical process. Numerical simulation appears to be the only practical method to fully understand its thermal, fluid and electromagnetic phenomena. In the past, many simulation models have been developed for one fusion welding method or another [1-17]. However, in most of these models, the deformation of the molten metal free surface was either ignored or greatly simplified. While the models can analyze the weld pool dynamics in gas tungsten arc welding (GTAW) or laser welding, they cannot describe

the surface deformation due to the arc pressure in all arc welding methods, the filler metal addition as in GTAW, the droplet impingement as in gas metal arc welding (GMAW), and the electron bombardment as in electron beam welding. These models are also incapable of predicting the weld reinforcement produced on the workpiece. According to a recent study [18], droplet transfer causes heavy deformation of the weld pool surface and is the most significant factor that determines the convection pattern in the weld pool of GMAW. Without proper modeling of the surface motion and the merging of multiple surfaces, the simulation will not be realistic.

Some numerical models simulate the free-surface-related droplet transfer and weld pool dynamics in GMAW [14-15,19-24]. Although these algorithms can be extended to other fusion welding processes, such as GTAW, laser welding and plasma-arc welding, the authors focused on the physical equations and boundary conditions, rather than discussion of the numerical methods. For example, most of these papers use Neumann boundary conditions on the free surface for heat flux or current density, but none explain how these boundary conditions are incorporated into the computation based on a staggered grid layout. The numerical models developed in these papers are either two-dimensional or axisymmetric, but do not explicitly explain how three-dimensional features, such as the welding speed, are integrated into the calculation. Computational efficiency is key to successful implementation. All surface tracking algorithms have limitations or numerical difficulties, but these papers rarely discuss possible algorithm improvement.

Without knowledge of the numerical details, others will find it difficult to implement these methods or duplicate their results. The high cost of the algorithm development will delay further improvement of these algorithms and prohibit the acceptance of numerical simulation as a standard alternative to the expensive experimental trial and error approach.

In this paper, an easy-to-follow numerical procedure is developed for the simulation of fusion welding processes where the influence of free surface motion is significant. This method can simulate the dynamic variations of the fluid, thermal and electromagnetic fields with high

resolutions with satisfactory computational expediency. It can also be integrated with microstructure and dendrite growth algorithms to generate a more sophisticated model to suit different applications.

This paper is organized as follows. Section 2 discusses some of the available surface tracking methods and fluid flow algorithms for fusion welding. Section 3 introduces the thermal and electromagnetic models. Section 4 shows a computation example of metal transfer and weld pool dynamics in gas metal arc welding. Section 5 summarizes the major contributions of this paper.

## 2. Surface tracking and fluid flow algorithms

In this section, available free-surface tracking methods and fluid flow algorithms are reviewed. Recommendations are made on their selection and improvement.

### *2.1. Overview of free surface tracking methods*

As described earlier, modeling weld pool oscillation requires tracking the molten metal free surface. Numerous methods developed to track free surfaces all have their strengths and weaknesses. Based on the nature of the mesh, these methods can be grouped into two categories: Lagrangian and Eulerian. Lagrangian methods use a deformable mesh that moves with the fluid. Each computational cell always contains the same fluid element as it moves and deforms [25,26]. With Eulerian methods, the numerical mesh is fixed in space and separate algorithms describe the position of the free surface. Popular methods in this category include the Marker-and-Cell (MAC) [27], the Volume-of-Fluid (VOF) [28], Front-Tracking [29] and level-sets [30,31].

While most recent GMAW models are based on the VOF method [14,15,20-22], the MAC and Front-Tracking methods have also simulated welding [19,23]. We recently conducted a benchmarking study to compare the VOF method and the Front Tracking method. While the Front Tracking method has the advantage of treating the entire domain as “one field” and its

explicit tracking of the fluid front seems more accurate than advection of marker functions, the following advantages of the VOF method makes it more suitable for modeling welding processes:

1) Its algorithms naturally conserve the mass of fluid.
2) It can easily handle large property variations across a free surface.
3) It automatically handles the topological changes of free surfaces, such as the breakup of liquid column into droplets and the merger of two fluid regions.

In this paper, numerical methods are developed primarily based on the two-dimensional and axisymmetric VOF algorithms. With some modifications, these methods can also model steady three-dimensional welding processes.

## *2.2 Fluid flow governing equations*

The welding simulation solves a set of coupled partial differential equations governing the fluid, thermal and electromagnetic fields. The equations include the continuity and Navier-Stokes equations. By assuming the molten metal is an incompressible fluid with constant viscosity, the fluid mechanics equations in axisymmetric swirl-free form are:

$$\frac{1}{r}\frac{\partial}{\partial r}\left(r v_r\right)+\frac{\partial v_z}{\partial z}=0 \tag{1}$$

$$\frac{\partial v_r}{\partial t}+\frac{1}{r}\frac{\partial\left(r v_r^2\right)}{\partial r}+\frac{\partial\left(v_r v_z\right)}{\partial z}= -\frac{1}{\rho}\frac{\partial p}{\partial r}+\frac{2}{r}\frac{\partial}{\partial r}\left(r\nu\frac{\partial v_r}{\partial r}\right)+\frac{\partial}{\partial z}\left(\nu\frac{\partial v_r}{\partial z}+\nu\frac{\partial v_z}{\partial r}\right)-2\nu\frac{v_r}{r^2}+\frac{f_r}{\rho} \tag{2}$$

$$\frac{\partial v_z}{\partial t}+\frac{1}{r}\frac{\partial\left(r v_r v_z\right)}{\partial r}+\frac{\partial\left(v_z^2\right)}{\partial z}= -\frac{1}{\rho}\frac{\partial p}{\partial z}+\frac{1}{r}\frac{\partial}{\partial r}\left(r\nu\frac{\partial v_r}{\partial z}+r\nu\frac{\partial v_z}{\partial r}\right)+\frac{\partial}{\partial z}\left(2\nu\frac{\partial v_z}{\partial z}\right)+\frac{f_z}{\rho} \tag{3}$$

## *2.3. Generation of computational mesh*

Using the finite-difference method, we discretize the equations on an Eulerian mesh of square cells covering the computational domain. Figure 1 shows the mesh layout generated for a GMAW process. Outside the physical domain, an extra layer of "ghost cells" ensures the boundary conditions are properly applied.

Although the VOF method has the capability to handle variable mesh sizes for local mesh refinement, we have found that the accuracy of variable meshes is often outweighed by complications that increase computational effort. As will be discussed later in the FLAIR algorithm, using variable meshes will also greatly increase the number of possible combinations of numerical situations at interfaces that make algorithms complex. For these reasons, uniform square meshes are used in this paper.

The transient fluid equations are solved using a "staggered grid" [32]. As shown in Figure 2, all the scalar field variables, including the fractional fluid volume $F$, the pressure $p$, the enthalpy $h$, the temperature $T$, the electric potential $V$ and the circumferential magnetic field $B_\theta$, are placed at the center of the cells; all vector field variables, including the velocity $\vec{v}$, the current density $\vec{J}$ and the body force $\vec{f}$, are placed at the midpoints of the cell boundaries.

## *2.4. Surface representation and reconstruction*

In the VOF algorithms, a function $F$ is defined as a scalar field variable for each computational cell to specify the fractional volume of a fluid occupying that cell. $F = 0.7$, for example, means 70% of the volume is occupied by the fluid. Away from interfaces, all cells will have either $F = 0$ or 1. Figure 3 illustrates how the $F$ function is distributed in relation to a free surface. By analyzing the $F$ functions in one cell and its 4 immediate neighboring cells, the algorithms judge which corner of the cell, if not full, is occupied by the fluid and where the free surface is located. The slope and curvature of the free surface can also be calculated by comparing the $F$ functions in its neighboring cells.

As the position of the free surface is specified by the $F$ function in each cell, the motion of the free surface can be tracked by updating $F$ in each cell according to the solution of the following transient equation:

$$\frac{DF}{Dt} = \frac{\partial F}{\partial t} + \underset{\vee}{v} \cdot \nabla F = 0 \tag{4}$$

where $D/Dt$ is the material derivative defined within the equation. $F$ moves with the fluid, and (4) acts as the kinematic boundary condition (KBC) for a free surface. When the KBC equation is integrated over a computational cell and a time step $\delta t$, the change in $F$ reduces to fluxes across its boundaries.

The original VOF algorithms [28] use a donor-acceptor algorithm to flux the fractional $F$ across cell boundaries. If a cell is located on the upstream side of a velocity vector, it is considered a donor cell; if it is on the downstream side of the velocity vector, it is an acceptor cell. Using the nomenclature of Hirt and Nichols [28], we call the radial direction horizontal and the axial direction vertical. Depending on whether the surface is more horizontal or vertical, the $F$ function is advected from the donor cell to the acceptor cell either horizontally or vertically in the amount given by the solution of the KBC equation, as shown in Figure 4(a). Because of this algorithm, the surface with a 45º slope is more likely to generate numerical errors and require bookkeeping techniques that will be discussed later.

Since the information about slope (first-order) and curvature (second-order) is not used during the fluid advection, the donor-acceptor algorithm only has zero$^{th}$-order accuracy. Since the introduction of the VOF method, many higher-order algorithms have been proposed, such as the first-order FLAIR [33] and Youngs' methods [34] and some second-order methods [35], where first- and second-order polynomials are employed to reconstruct the free surface. These methods partially correct errors caused by surfaces with a 45º slope.

We use the FLAIR method in this paper since it improves the accuracy in the advection of *F* and its algorithms are more efficient and easier to implement than second-order methods.

In the FLAIR method as shown in Figure 4(b), the free surface is represented by a set of line segments fitted at the boundary of two neighboring cells. The possible arrangements of the two cells are classified into nine cases. Criteria is developed to distinguish these cases, and a separate algorithm computes the flux across the boundary between the two cells for each case.

Figure 5 shows an example flux calculation in the FLAIR algorithms. This type of surface structure appears when $f_a \le 3 f_b$ and $3 f_a - f_b \le 2$. When the free surface is represented by $y = a x + b$ and the velocity on the boundary of the two cells, *u*, is in the positive *x* direction, the flux of fluid from the left cell to the right cell is:

$$\delta f^{+} = \frac{u \delta t}{\delta h}\left( a + \frac{b}{\delta h} - \frac{a}{2}\frac{u \delta t}{\delta h} \right) \tag{5}$$

where $\delta h = \delta x = \delta y$ is the grid size. If the velocity *u* is in the negative *x* direction, the flux of fluid from the right cell to the left cell is

$$\delta f^{-} = \frac{u \delta t}{\delta h}\left( a + \frac{b}{\delta h} + \frac{a}{2}\frac{u \delta t}{\delta h} \right). \tag{6}$$

A problem of the VOF method is that nonphysical voids or fluid filaments are often generated and propagate throughout the computational domain. Wang and Tsai [22] discussed the "particles" above the weld pool and the "voids" in the weld pool and concluded that they were caused by numerical errors. To suppress these voids and filaments, two bookkeeping strategies can be used. One strategy improves the advection algorithms to prevent the creation of the filaments and voids. This can be achieved by using higher-order reconstruction algorithms such as the FLAIR method or by limiting the fluid fluxed to an empty cell. The second strategy fine-tunes the $F$ values when the advection is completed. This can be achieved by setting upper and lower bounds for the partially filled cells or by filling the interior cells with the fluid in the surface cells.

## *2.5. Surface stress*

The stress tensor in an incompressible Newtonian fluid is

$$\tau_{ij} = -p\,\delta_{ij} + \mu\left(\frac{\partial v_i}{\partial x_j} + \frac{\partial v_j}{\partial x_i}\right) \tag{7}$$

indicating the momentum flux in the $j^{\text{th}}$-direction normal to the $i^{\text{th}}$-direction.

The major surface forces in welding processes include the surface tension, the arc pressure, the Marangoni stress and the gas drag. The surface tension and arc pressure are in the normal direction while the Marangoni stress and gas drag are in the tangential direction. Therefore, the normal and tangential surface stresses can be written as:

$$\tau_{nn} = -p + 2\mu\frac{\partial v_n}{\partial n} = -\gamma\left(\frac{1}{R_1} + \frac{1}{R_2}\right) - p_{arc} \tag{8}$$

$$\tau_{nm} = \mu\left(\frac{\partial v_n}{\partial s} + \frac{\partial v_s}{\partial n}\right) = \frac{d\gamma}{dT}\frac{\partial T}{\partial s} + \tau_{drag} \tag{9}$$

In a two-dimensional space, the surface stresses take the following form [36]:

$$-p + 2\mu\left[n_x n_x\frac{\partial u}{\partial x} + n_x n_y\left(\frac{\partial u}{\partial y} + \frac{\partial v}{\partial x}\right) + n_y n_y\frac{\partial v}{\partial y}\right] = -\gamma\left(\frac{1}{R_1} + \frac{1}{R_2}\right) - p_{arc} \tag{10}$$

$$\mu\left[2n_x s_x\frac{\partial u}{\partial x} + (n_x s_y + n_y s_x)\left(\frac{\partial u}{\partial y} + \frac{\partial v}{\partial x}\right) + 2n_y s_y\frac{\partial v}{\partial y}\right] = \frac{d\gamma}{dT}\frac{\partial T}{\partial s} + \tau_{drag} \tag{11}$$

Application of surface stress in the VOF algorithms sets pressure values at surface cells and velocity values at locations adjacent to the surface cell. If a surface cell has only one side open to an empty cell, the free surface is considered either horizontal or vertical [37], and the surface stresses become:

$$-p + 2\mu\frac{\partial v}{\partial y} = -\gamma\left(\frac{1}{R_1} + \frac{1}{R_2}\right) - p_{arc} \tag{12}$$

$$\mu\left(\frac{\partial v}{\partial x}+\frac{\partial u}{\partial y}\right)=\frac{d\gamma}{dT}\frac{\partial T}{\partial x}+\tau_{drag} \tag{13}$$

Figure 6(a) shows an example where the surface cell $P$ has one side open to an empty cell and the free surface is considered horizontal. The pressure $P_i^j$ and velocities $V_i^{j+1/2}$, $U_{i-1/2}^{j+1}$ and $U_{i+1/2}^{j+1}$ need to be specified such that the surface stress conditions (8) and (9), as well as the continuity equation, are satisfied:

$$V_i^{j+1/2}=V_i^{j-1/2}-\left(U_{i+1/2}^{j}-U_{i-1/2}^{j}\right)\frac{\delta y}{\delta x} \tag{14}$$

$$P_i^j=\gamma\left(\frac{1}{R_1}+\frac{1}{R_2}\right)+p_{arc}+2\mu\frac{V_i^{j+1/2}-V_i^{j-1/2}}{\delta y} \tag{15}$$

$$U_{i-1/2}^{j+1}=U_{i-1/2}^{j}+\frac{\delta y}{\mu}\left[\frac{d\gamma}{dT}\frac{T_P-T_W}{\delta x}+\tau_{drag}-\mu\frac{V_i^{j+1/2}-V_{i-1}^{j+1/2}}{\delta x}\right] \tag{16}$$

$$U_{i+1/2}^{j+1}=U_{i+1/2}^{j}+\frac{\delta y}{\mu}\left[\frac{d\gamma}{dT}\frac{T_E-T_P}{\delta x}+\tau_{drag}-\mu\frac{V_{i+1}^{j+1/2}-V_i^{j+1/2}}{\delta x}\right] \tag{17}$$

If a surface cell has two sides open to empty cells, the normal direction of the free surface is assumed to be at 45º between the open sides [37]. The normal and tangential stresses become:

$$-p\pm\mu\left(\frac{\partial u}{\partial y}+\frac{\partial v}{\partial x}\right)=-\gamma\left(\frac{1}{R_1}+\frac{1}{R_2}\right)-p_{arc} \tag{18}$$

$$\mu\left(-\frac{\partial u}{\partial x}+\frac{\partial v}{\partial y}\right)=\frac{d\gamma}{dT}\frac{\partial T}{\partial s}+\tau_{drag} \tag{19}$$

where the sign in (18) is chosen equal to the sign of $n_x n_y$. Figure 6(b) shows an example of this case, where the surface cell $P$ has two sides open to empty cells and the normal direction of the free surface is considered as $-n_x=n_y=\frac{1}{\sqrt{2}}$. The pressure $P_i^j$ and velocities $V_i^{j+1/2}$ and $U_{i-1/2}^{j}$ are specified as follows:

$$V_i^{j+1/2}=V_i^{j-1/2}+\frac{\delta y}{2\mu}\left(\frac{\partial\gamma}{\partial T}\frac{T_E-T_S}{\sqrt{2}\,\delta x}+\tau_{drag}\right) \tag{20}$$

$$U_{i-1/2}^{j} = U_{i+1/2}^{j} + \left(V_i^{j+1/2} - V_i^{j-1/2}\right)\frac{\delta x}{\delta y} \tag{21}$$

$$P_i^j = \gamma\left(\frac{1}{R_1} + \frac{1}{R_2}\right) + p_{arc} - \mu\left[\frac{U_{i+1/2}^{j} - U_{i+1/2}^{j-1} + U_{i-1/2}^{j} - U_{i-1/2}^{j-1}}{2\delta y} + \frac{V_{i+1}^{j+1/2} - V_i^{j+1/2} + V_{i+1}^{j-1/2} - V_i^{j-1/2}}{2\delta x}\right] \tag{22}$$

A cell with three sides open to empty cells is rare. In that case, we simply allow the velocities at the two opposite empty sides to take on the values of the adjacent velocities inside the fluid, and compute the velocity at the third empty side and the pressure of the cell based on the continuity equation and (15).

## *2.6. Solving the continuity and momentum equations*

The original VOF algorithms [28] use two steps to solve the coupled momentum (Navier-Stokes) and continuity equations. The first step predicts the velocity components using the momentum equation, and the second step corrects the pressure term and the velocity components using the continuity equation. A weakness of this method is that when successive iterations correct the pressure and velocity components, the momentum equation is not involved. Therefore, when a converged solution is found, the momentum equation is not accurately satisfied. In addition, the method requires a large number of iterations in each time step and is not considered efficient.

The most widely used method that *simultaneously* solves the momentum and continuity equations is Patankar's SIMPLE (Semi-Implicit Method for Pressure Linked Equations) method [32]. Later improvements to the SIMPLE algorithms include the SIMPLER method [32], the SIMPLEC method [38] and the PISO method [39]. While benchmarking studies [40,41] show that each of the improved methods has its own advantages, Chao, et al. [42] indicates that SIMPLEC is the most efficient and stable method for solving complex turbulent flow. Although

the flow in a fusion welding process is considered laminar ( $\mathrm{Re} = \rho v_{\max} D/\mu < 2000$ ), we find SIMPLEC requires the least modification to the SIMPLE algorithm and is easier to implement.

### *2.7. Some numerical techniques*

In the development of numerical algorithms, we find it convenient if two flag variables are defined for each cell to identify the physical entity and its surface that the cell is located. We use OBJECT_NAME(i,j) to identify the cell object , such as the top-layer workpiece, the bottom-layer workpiece, the welding wire or the molten droplet. We use SURFACE_NAME(i,j) to identify the surface of the object , such as the top or bottom surface of a workpiece. By doing so, different boundary conditions and algorithms are easily applied to improve efficiency.

In VOF algorithms, a flag variable NF(i,j) indicates whether a cell is a surface or an interior cell, and, if it is a surface cell, the cell side adjacent to the bulk fluid. In some complex situations, we need to know which side of a non-surface cell is adjacent to the main fluid body. Since computer memory is no longer a big concern in today's computing environment, we recommend that each variable only have one function. In this case, we split the variable NF(i,j) into two field variables: one called POSITION(i,j) to indicate if the cell is on the free surface, inside a fluid, or outside the fluid; and the other called NEIGHBOR(i,j) to indicate the neighboring cell in the main fluid body. With this arrangement, all cells near the free surface have NEIGHBOR(i,j) values, whether they are surface cells or interior cells.

## 3. Integration of thermal and electromagnetic models

Fusion welding is not only a fluid problem, but also involves complex thermal and electromagnetic phenomena. Simulation of the process requires an integration of the thermal and electromagnetic models into the fluid flow and surface tracking algorithms.

## *3.1. Thermal equation and phase change problem*

For an incompressible substance, the energy equation is:

$$\frac{Dh}{Dt} = \nabla \cdot k \nabla T + q''' \tag{23}$$

where $h$ is the enthalpy, $k$ is the thermal conductivity and $q'''$ is heat generation . Equation (23) is known as the enthalpy formulation of the energy equation, and for constant specific heat at constant pressure $c_p$ it can be transformed to a temperature formulation as:

$$\rho c_p \frac{DT}{Dt} = \nabla \cdot k \nabla T + q''' \tag{24}$$

where only one unknown, $T$ , remains.

The temperature formulation (24) was used by Chan, Mazumder and Chen to model a laser melted weld pool [4]. Solution of the equation typically requires three steps:

(1) Determining the location of the solid-liquid interface based on the temperature distribution obtained in the previous time step;

(2) Applying a heat balance boundary condition on the interface [43]:

$$k_s \nabla T_s \cdot \vec{n} - k_l \nabla T_l \cdot \vec{n} = \rho L \vec{v} \cdot \vec{n} ; \tag{25}$$

(3) Solving the energy equation for solid and liquid *separately*.

In addition to the complexity of the procedure, the discretized representation of solid-liquid interface may introduce extra numerical temperature errors.

The enthalpy formulation, on the other hand, eliminates the need to explicitly track the solid-liquid interface or apply heat interface balance conditions because energy is conserved over the entire solid-liquid system. This method used here was introduced to the modeling of weld pools by Kou and Sun [5].

For a material whose phase change occurs at a constant temperature, the temperature-enthalpy relationship is:

$$T = \begin{cases} T_m + \dfrac{h}{c_s} & (h \le 0) \\ T_m & (0 < h < L) \\ T_m + \dfrac{h - L}{c_l} & (h \ge L) \end{cases} \tag{26}$$

where $T_m$ is the melt temperature, $L$ is the latent heat, and the subscripts $s$ and $l$ on $c$ indicate specific heats for the solid and liquid, respectively. For those materials whose phase change occurs over a temperature range, the relationship becomes:

$$T - T_s = \begin{cases} \dfrac{h}{c_s} & (h \le 0) \\ \dfrac{h(T_l - T_m)}{L + c_m(T_l - T_m)} & (0 < h < L + c_m(T_l - T_m)) \\ \dfrac{h}{c_l} - \dfrac{L + (c_m - c_l)(T_l - T_s)}{c_l} & (h \ge L + c_m(T_l - T_m)) \end{cases} \tag{27}$$

The enthalpy formulation (23) contains two dependent variables, the enthalpy $h$ and the temperature $T$. Due to the nonlinearity in the $h$-$T$ relationship, some strategies, such as those developed by Voller, et al. [44] and Cao, et al. [45], should be used to solve the equation. In this paper, we use Cao, et al.'s method for its numerical simplicity.

When the position of the free surface (both the liquid-gas interface and the solid-gas interface) is determined using the VOF (or FLAIR) method, boundary conditions can be applied on the surfaces and the momentum, energy and current equations can be solved within the *generalized liquid phase*. A large effective viscosity [5] can be used for the cells that have temperatures lower than the melting (or the liquidus) temperature. We set the large artificial viscosity at $10^8$ times the viscosity of the nearby liquid to virtually eliminate the relative motion in the solid phase.

## *3.2. Simulation of the electromagnetic field*

In the arc welding process, the current-carrying molten metal, under the influence of self-induced magnetic field, generates an electromagnetic force that affects the motion of the molten metal. The electromagnetic force per unit mass is determined by the Lorenz force law:

$$\vec{f} = \vec{J} \times \vec{B}. \tag{28}$$

For welding applications where the electromagnetic field is considered quasi-steady, the magnetic field can be solved using a simplified Maxwell's equation:

$$\oint \vec{B} \cdot \mathrm{d}\vec{s} = \mu_0 I \tag{29}$$

stating that the line integral of the magnetic field around any closed path equals to the total current passing through the closed path.

From the analysis above, we find that both terms in (28) require knowledge of the current density distribution within the molten fluid. The current flow in the fluid with no ability to store charge is governed by the Laplace equation:

$$\nabla \cdot (\sigma \nabla V) = 0 \tag{30}$$

Although this equation has a very simple form, it is the most time-consuming equation in the entire simulation. The slow convergence of the numerical iteration is caused by the following two factors:

(1) The numerical iteration is very sensitive to the Neumann boundary conditions located on a curved and moving free surface whose shape can be arbitrary;

(2) Unlike the energy and momentum equations, electric potential is not a function of time. Any topological change on the boundary instantly affects the electric potential everywhere.

To increase the computation speed, we introduce an artificial transient term to the Laplace equation and make it a diffusion equation:

$$\frac{\partial V}{\partial t} = \vartheta \nabla \cdot (\sigma \nabla V) \tag{31}$$

where $\vartheta$ is a positive diffusion constant with a unit of $\Omega \cdot m^3/\text{sec}$. For given boundary conditions, the unique solution of a diffusion equation evolves to a steady state as $t \to \infty$ regardless of its initial conditions.

Selection of $\vartheta$ value is determined using numerical trial-and-error. $\vartheta$ should be large enough to ensure acceleration of the iteration, without affecting the result.

### *3.3. Applying boundary conditions on curved surfaces*

In welding simulations, Neumann boundary conditions are often applied on the fluid surfaces. For example, Choi et al. [15] assumed that the current density passing through the free surface of molten metal is zero, or $\partial V/\partial n = 0$. Fan and Kovacevic [21] assumed the thermal condition on the weld pool surface without arc heating is $-k\ \partial T/\partial n = h_c(T - T_\infty)$ and that the free surface current flux $\partial V/\partial n$ obeys a Gaussian distribution.

Neumann conditions are applied by interpolating the variable, e.g. the voltage, near the fluid surface, as shown in Figure 8. Suppose the dark line is a free surface that passes through a cell *o* and its slope *m* is known. We first reorient the cell such that the fluid is below the surface and its right neighboring cell contains more fluid than its left neighboring cell, as shown in the figure. During the reorientation, the slope may change sign or take its reciprocal value. We designate the cell below the surface cell as *b*, and the cell next to *b* on the right as *a*. The goal is to determine the voltage of cell *o* ($V_o$) such that the current density normal to the free surface satisfies a prescribed value ($J_n$). To achieve this, we need to interpolate the voltage at cells *a* and *b*. Suppose letters *o*, *a* and *b* also represent the center points of the cells. After drawing two lines to connect $\overline{ob}$ and $\overline{ba}$, we draw another line starting from o and perpendicular to the free surface and designate the point where the new line intersects with $\overline{ba}$ as point *c*. Letting $\angle boc = \alpha$, then $\alpha = \tan^{-1} m$. Interpolation on $\overline{ba}$ gives:

$$\frac{V_c - V_b}{\overline{cb}} = \frac{V_a - V_b}{\overline{ba}} \tag{32}$$

or

$$V_c = V_b + (V_a - V_b)\frac{m\delta y}{\delta x} \tag{33}$$

where all terms on the right hand side are known, and so is $V_c$. Since $\overline{ca}$ is normal to the free surface, we can approximate $J_n$ by:

$$J_n = \sigma \frac{V_c - V_o}{\overline{co}} \tag{34}$$

or

$$V_o = V_c - J_n \frac{\overline{co}}{\sigma} = V_c - J_n \frac{\delta y}{\sigma \cos\alpha}. \tag{35}$$

Therefore, the voltage in the surface cell becomes:

$$V_o = V_b + (V_a - V_b)\frac{m\delta y}{\delta x} - J_n \frac{\delta y}{\sigma \cos\alpha} \tag{36}$$

The same procedure can also be applied to determine the enthalpy in surface cells.

## 4. Simulation procedure and example

To simulate a fusion welding process, we consider the problem as a two-phase system: one is the gas phase, including the arc plasma, the shielding gas and the air; the other is a *generalized liquid phase*, including the melted and unmelted metals. The two phases are separated by one or more free surfaces, whose positions are dynamically tracked by the VOF or FLAIR algorithms. In the *generalized liquid phase*, enthalpy-based energy equation determines the temperature distribution. If a cell has a temperature lower than the melting point (or the solidus temperature), it is considered as an unmelted (or solidified) cell and its viscosity is replaced by an *effective-viscosity*, $10^8$ times that of the surrounding fluid. With the *effective-viscosity*, when the Navier-Stokes Equation is solved for the *generalized liquid phase*, the relative motion in the solid region is virtually eliminated. The electromagnetic equations are also solved in the generalized liquid phase. The electromagnetic force moves the fluid and the Joule

heating increases the local temperature. Surface stresses, including the surface tension, arc pressure, Marangoni effect and gas drag are applied on the surface cells as boundary conditions to the governing equations of the *generalized liquid phase*. These boundary conditions may be Dirichlet, Neumann or mixed. The enthalpy formulation with effective viscosity requires no interface conditions at the solid-liquid boundaries. We do not even need to know the actual locations of the boundaries. For a two-dimensional model, the welding speed is considered as a function that causes the external heat source to gradually move into the welding area and gradually move out of the welding area.

Figure 9 is a flow chart of the computational procedure.

(1) Geometric, physical, material and control parameters, as well as the welding conditions, are first read into memory.

(2) A computational mesh is generated and field variables are initialized based on initial conditions.

(3) Navier-Stokes equations, as well as the continuity equation, are solved for velocity and pressure distributions using the SIMPLEC algorithm.

(4) The FLAIR method determines the new positions of the free surface by solving the KBC equation.

(5) Due to numerical instability, steps (3) and (4) may not give converging solutions. When that happens, the time increment is reduced by 20%, and steps (3) to (5) are repeated.

(6) The free surface is assessed and the values of the identification variables for each cell are determined.

(7) The surface curvature and stresses are calculated.

(8) The Laplace equation determines the voltage distribution. The current density, magnetic field and electromagnetic force are calculated based on Ohm's law, the Maxwell Equation and the Lorenz force law.

(9) The energy equation is solved for enthalpy and temperature distributions.

(10) Temperature-dependent material properties are updated and the large effective viscosity is assigned to cells whose temperatures are lower than the melting point.

(11) The process advances to the next time step with intermediate results saved. The new values of fractional volume, velocity, pressure and enthalpy are now considered as "old" values. If the time increment was reduced previously, it is increased by 10% and gradually returns to the preset value. Steps (3) to (11) are repeated until the desired termination time is reached.

Figure 10 shows an example of the simulation for a GMAW process with a consumable electrode wire. The material properties are listed in Table 1. The process is modeled axisymmetrically with the following boundary conditions:

The top computational surface is considered a fluid inlet, whose voltage equals the given welding voltage and temperature equals the ambient temperature due to its long distance to the melting tip:

$$v_z = -v_{feed},\ v_r = 0,\ T = T_{ambient}, \text{ and } V = U$$

The bottom surface is a free-slip wall that is adiabatic and electrically grounded:

$$\frac{\partial v_r}{\partial z} = 0,\ v_z = 0,\ \frac{\partial T}{\partial z} = 0, \text{ and } V = 0$$

The inner surface is the symmetry axis:

$$v_r = 0,\ \frac{\partial v_z}{\partial r} = 0,\ \frac{\partial T}{\partial r} = 0, \text{ and } \frac{\partial V}{\partial r} = 0$$

The outer surface is also a free-slip wall that is adiabatic and electrically grounded:

$$v_r = 0,\ \frac{\partial v_z}{\partial r} = 0,\ \frac{\partial T}{\partial r} = 0, \text{ and } \frac{\partial V}{\partial r} = 0$$

On the free surfaces of the weld pool, we assume the current density and heat flux obey the Gaussian distribution:

$$\sigma \frac{\partial V}{\partial z} = \frac{I}{2\pi \sigma_j^{\,2}} \exp\left( -\frac{r^2}{2\sigma_j^{\,2}} \right) \tag{37}$$

$$k \frac{\partial T}{\partial z} = \frac{\eta_p \eta U_{arc} I}{2\pi \sigma_q^{\,2}} \exp\left( -\frac{r^2}{2\sigma_q^{\,2}} \right) - h_c (T - T_\infty) . \tag{38}$$

On the free surface of the welding wire, we assume the current density and heat flux are linear along the vertical direction [24]:

$$\sigma \frac{\partial V}{\partial n} = -\frac{I \cdot z}{\int z \cdot dA} \tag{39}$$

$$k \frac{\partial T}{\partial n} = \frac{\eta_d \eta U I \cdot z'}{\int z' \cdot dA} . \tag{40}$$

The surface tension is included in the calculation, while other stresses are ignored.

Figure 11 shows the simulated procedure of droplet growth and detachment in globular and spray modes. For illustration purpose, only one transfer period is displayed in each figure, and irregular time intervals are used. Figure 11 shows that melting front on the wire is not flat and its shape is determined by the heat convection between the wire and the droplet. Since the wire is primarily melted by resistive heating, anode reaction, and arc heating, the wire surface directly exposed to the arc tends to melt faster than the interior metal. Therefore, the melting interface usually turns out to be convex. However, in the neighborhood of the detachment, the center of the melting interface is depressed due to an upward recoil flow caused by the unbalanced surface tension. When that happens, the melting front becomes crater-shaped as shown in the last plot of Figure 11.

Figure 12 shows a simulation of continuous droplet transfer and weld pool development in spray mode at 300A. Through impingement the molten droplets transfer mass, momentum and energy to the weld pool. It seems that while the convection of weld pool is driven by many factors, the impingement of molten droplets is the most significant one that determines the fluid motion in the weld pool. When a droplet impacts into the weld pool, the weld pool surface

deformed drastically and heat carried by the droplet is transferred towards the root of the weld pool, resulting in a finger-shaped geometry. Analogous to the forced vibration in dynamics, the surface oscillation of the weld pool is synchronized with the periodic excitation from the droplet impingement. The simulation results presented here are in broad agreement with experiments[18].

## 5. Conclusions

This paper developed a numerical procedure for the simulation of fusion welding processes where free surfaces are involved. The VOF method is used to track the motion of the molten metal free surfaces, but its surface advection and reconstruction algorithm (the donor-acceptor algorithm) is replaced by the more accurate FLAIR algorithm. Surface stresses, including the surface tension, Marangoni stress, arc pressure and gas drag, are applied on the free surface. The SIMPLEC method is used to solve the coupled momentum and continuity equations. Thermal equations are integrated in the algorithm using the Enthalpy method, eliminating the need for explicitly tracking the melting front. Electromagnetic fields are calculated by first solving the Laplace equation for electrical potential, where an artificial transient term is introduced to expedite the computation. Numerical techniques, such as the application of boundary conditions on curved surfaces, are also described. Based on these details, a general numerical procedure is presented. While a simulation example is shown for gas metal arc welding, the numerical methods can be also applied to gas tungsten welding, laser welding and plasma arc welding.

Droplet growth and detachment in globular and spray modes are simulated using the numerical procedure presented in this paper. It is observed that the shape the melting front on the wire is determined by the heat convection between the wire and the droplet. Both convex and crater-shaped melting interfaces are presented in the same transfer cycle. Effects of the droplet impingement on the weld pool development are studied for spray transfer. The mass,

momentum, and enthalpy carried by the droplets significantly affects the heat convection mode in the weld pool and result in a finger-shaped geometry. The simulation is in good agreement with experiments.

## Acknowledgement

This research is supported by General Motors Corporation through the GM Collaborative Research Laboratory at the University of Michigan (Grant number DRDA013142). The authors would like to express their sincere thanks to Dr. Samuel P. Marin and Dr. Pei-Chung Wang from GM R&D for their support and comments.

## References


[1] Andrews JG, Craine RE. Fluid flow in a hemisphere induced by a distributed source of current, *Journal of Fluid Mechanics* 1978; 84: 281-290.

[2] Atthey DR, A mathematical model for fluid flow in a weld pool at high currents. *Journal of Fluid Mechanics* 1980; 98: 787-801.

[3] Oreper GM, Eagar TW, Szekely J. Convection in arc weld pools. *Welding Journal* 1983; 63: 307-312.

[4] Chan C, Mazumder J, Chen JJ. A two-dimensional transient model for convection in laser melted pool. *Metallurgical Transactions A* 1984; 15: 2175-2184.

[5] Kou S, Sun DK. Fluid flow and weld penetration in stationary arc welds. *Metallurgical Transactions A* 1985; 16: 203-213.

[6] Zacharia T., Eraslan AH, Aidun DK, David SA. 3-dimensional transient model for arc-welding process. *Metallurgical Transsactions B* 1989; 20: 645-659.

[7] Kou S., Wang YH. Weld pool convection and its effects. *Weld.ing Journal* 1986; 65: 63-70.

[8] Tsao S, Wu CS. Fluid flow and heat transfer in GMA weld pools. *Welding Journal* 1988; 67: 70-75.

[9] Zacharia T, David SA, Vitek JM, Debroy T. Modeling of interfacial phenomena in welding. *Metallurgical Transactions B* 1990; 21: 600-603.

[10] Kim YS, McEligot DM, Eagar TW. Analysis of electrode heat transfer in gas metal arc welding. *Welding Journal* 1991; 70: 20-31.

[11] David SA, Debroy T, Vitek JM. Phenomenological modeling of fusion-welding processes. MRS Bulletin 1994; 19: 29-35.

[12] Kim JW, Na SJ. A study on the three-dimensional analysis of heat and fluid flow in gas metal arc welding using boundary-fitted coordinates. *Journal of Engineering for Industry, Transactions of the ASME* 1994; 116: 78-85.

[13] Ushio M, Wu CS. Mathematical modeling of three-dimensional heat and fluid flow in a moving gas metal arc weld pool, *Metallurgical and Material Transactions B* 1997; 28: 509-516.

[14] Choi SK, Yoo CD, Kim YS. Dynamics simulation of metal transfer in GMAW, Part 1: globular and spray transfer modes. *Welding Journal* 1998; 77: 38-44.

[15] Choi SK, Ko SH, Yoo CD, Kim YS. Dynamic simulation of metal transfer in GMAW - Part 2: short-circuit transfer mode. *Welding Journal* 1998; 77: 45-51.

[16] Cao ZN, Dong P. Modeling of GMA weld pools with consideration of droplet impact. *Journal of Engineering Materials and Technology, Transactions of the ASME* 1998; 120: 313-320.

[17] Hong T, Debroy T, Babu SS, David SA. Modeling of inclusion growth and dissolution in the weld pool. *Metallurgical and Material Transactions B* 2000; 31: 161-169.

[18] Wang F, Hou WK, Hu SJ, Kannatey-Asibu E, Schultz WW, Wang PC. Numerical characterization of weld pool dynamics in gas metal arc welding. in preparation for *Journal of Manufacturing Science and Engineering – Transactions of the ASME*.

[19] Maruo H, Hirata Y, Goto N. Bridging transfer phenomena of conductive pendent drop - the effects of electromagnetic pinch force on the bridging transfer. *Quarterly Journal of the Japan Welding Society* 1992; 10: 43-50.

[20] Haidar J, Lowke JJ. Predictions of metal droplet formation in arc welding. *Journal of Physics D: Applied Phycis* 1996; 29: 2951-2960.

[21] Fan HG, Kovacevic R. Droplet formation, detachment, and impingement on the molten pool in gas metal arc welding. *Metallurgical and Material Transactions B* 1999; 30: 791-801.

[22] Wang Y, Tsai HL. Impingement of filler droplets and weld pool dynamics during gas metal are welding process. *International Journal of Heat and Mass Transfer* 2001; 44: 2067-2080.

[23] Xu G, Kannatey-Asibu E, Schultz WW, Wang PC. Simulation of gas metal arc welding short circuiting transfer using a front tracking method. *Proceedings of IMECE'02*, New Orleans, Louisiana, November 17-22, 2002.

[24] Wang F, Hou WK, Hu SJ, Kannatey-Asibu E, Schultz WW, Wang PC. Modeling and analysis of metal transfer in gas metal arc welding. Journal of Physics D: Applied Physics 2003; 36: 1143-1152..

[25] Hirt CW, Cook JL, Butler TD. A Lagrangian method for calculating the dynamics of an incompressible fluid with free surface. Journal of Computational Physics 1970; 5: 103-124.

[26] Crowley WP. FLAG: A free-Lagrange method for numerically simulating hydrodynamic flows in two dimensions. *Lecture Notes in Physics* 1971; 8: 37-43.

[27] Harlow FH, Welch JE. Numerical calculation of time-dependent viscous incompressible flow of fluid with free surface. *Physics of Fluids* 1965; 8: 2182-2189.

[28] Hirt CW, Nichols BC. Volume of fluid (VOF) method for the dynamics of free boundaries. *Journal of Computational Physics* 1981; 39: 201-225.

[29] Unverdi SO, Tryggvason G. A front-tracking method for viscous, incompressible, multi-fluid flows. Journal of Computational Physics 1992; 100: 25-37.

[30] Sussman M, Smereka P, Oscher S. A level set approach for computing solutions to incompressible two-phase flow. Journal of Computational Physics 1994; 114: 146-159.

[31] Sethian JA. *Level Set Methods*. Cambridge University Press: Cambridge, UK, 1996.

[32] Patankar SV. *Numerical Heat Transfer and Fluid Flow*. Hemisphere: New York, 1980.

[33] Ashgriz N, Poo JY. FLAIR: Flux line-segment model for advection and interface reconstruction. Journal of Computational Physics 1991; 93: 449-468.

[34] Youngs DL Time-dependent multi-material flow with large fluid distortion, *Numerical Methods for Fluid Dynamics*, edited by Morton and Baines. Academic Press: New York, 1982.

[35] Kim S, No HC. Second-order model for free surface convection and interface reconstruction. *International Journal for Numerical Methods in Fluids* 1998; 26: 79-100.

[36] Hirt CW, Shannon JP. Free-surface stress conditions for incompressible-flow calculations. Journal of Computational Physics 1968; 2: 403-411.

[37] Nichols BD, Hirt CW. Improved free surface boundary conditions for numerical incompressible-flow calculations. Journal of Computational Physics 1971; 8: 434-448.

[38] Van Doormaal JP, Raithby GD. Enhancements of the SIMPLE method for predicting incompressible fluid flows. *Numerical Heat Transfer* 1984; 7: 147-163.

[39] Issa RI, Gosman AD, Watkins AP. The computation of compressible and incompressible recirculating flows by a non-iterative implicit scheme. Journal of Computational Physics 1986; 62: 66-82.

[40] Van Doormaal JP, Raithby GC. Evaluation of the segregated approach for predicting incompressible fluid flows. *Proceedings of 1985 ASME National Heat Transfer Conference*, Denver, Colorado, 1985.

[41] Jang DS, Jetli R, Acharya S. Comparison of the PISO, SIMPLER, and SIMPLEC algorithms for the treatment of the pressure-velocity coupling in steady flow problems. *Numerical Heat Transfer* 1986; 10: 209-228.

[42] Chao YC, Ho WC. Behaviour of five solution algorithms on turbulent calculations. *Communications in Applied Numerical. Methods* 1989; 5: 253-261.

[43] Voller VR. An overview of numerical methods for solving phase change problems. *Advances in Numerical Heat Transfer* 1996; 1: 341-380.

[44] Voller VR, Prakash C. A fixed grid numerical modeling methodology for convection-diffusion mushy region phase-change problems. *International Journal of Heat and Mass Transfer* 1987; 30: 1709-1719.

[45] Cao Y, Faghri A, Chang WS. A numerical analysis of Stefan problems for generalized multi-dimensional phase-change structures using the enthalpy transforming model. International Journal of Heat and Mass Transfer 1989; 32: 1289-1298.

**List of Figures**



**List of Tables**

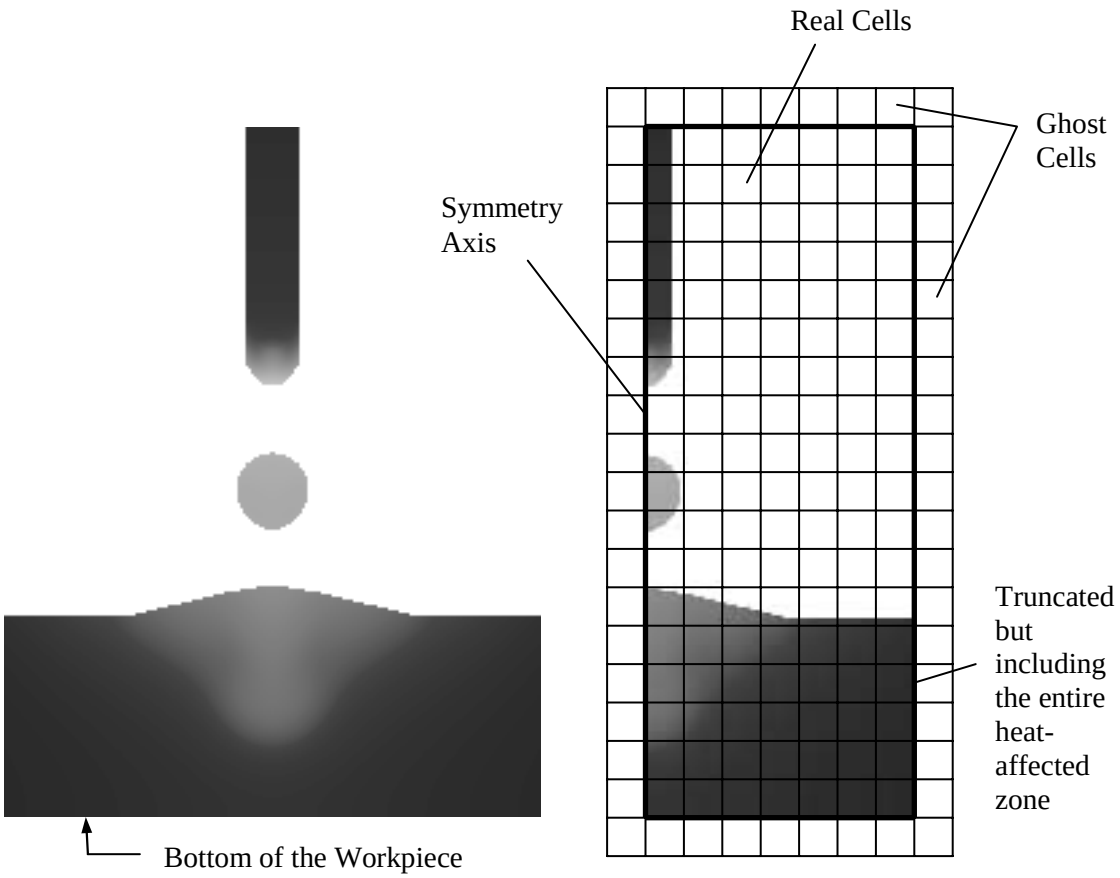


(a) GMAW process (b) Mesh layout

Figure 1. Schematic of mesh layout. The figures indicate how the real and "ghost" cells are located; the actual mesh is typically 20 times finer.

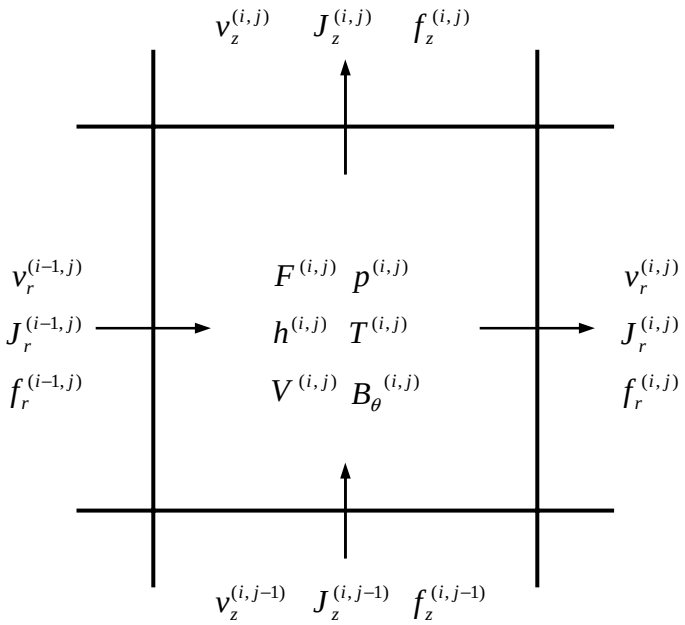


Figure 2. Layout of discretized field variables.

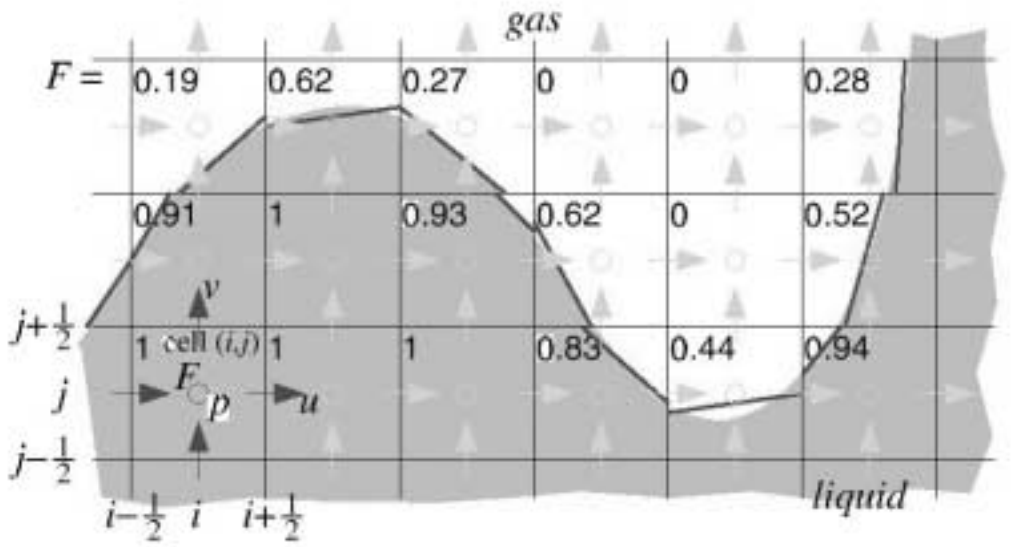


Figure 3. Surface representation in the VOF method. Fraction numbers indicate the ratio of volume occupied by the liquid.

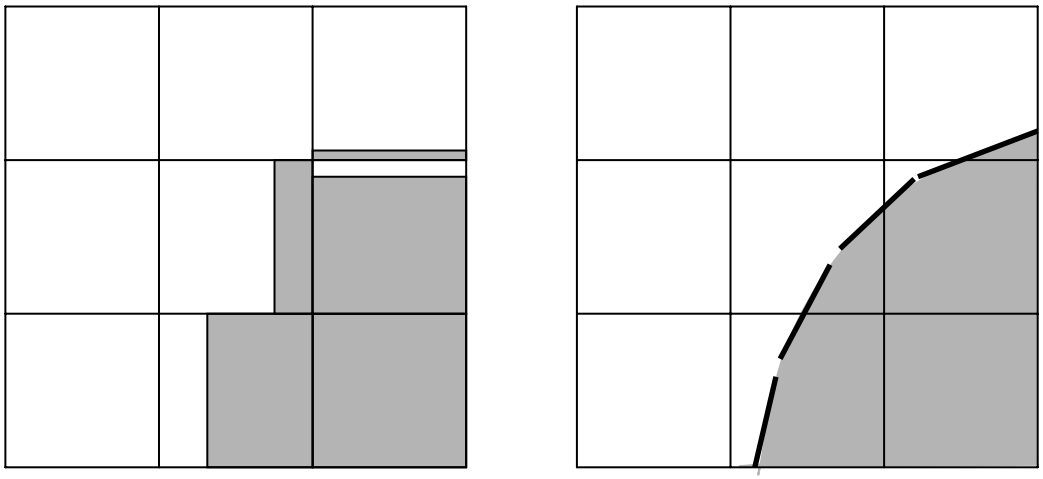

(a) VOF Method (b) FLAIR Method

Figure 4. Comparison of surface reconstruction in VOF and FLAIR methods.

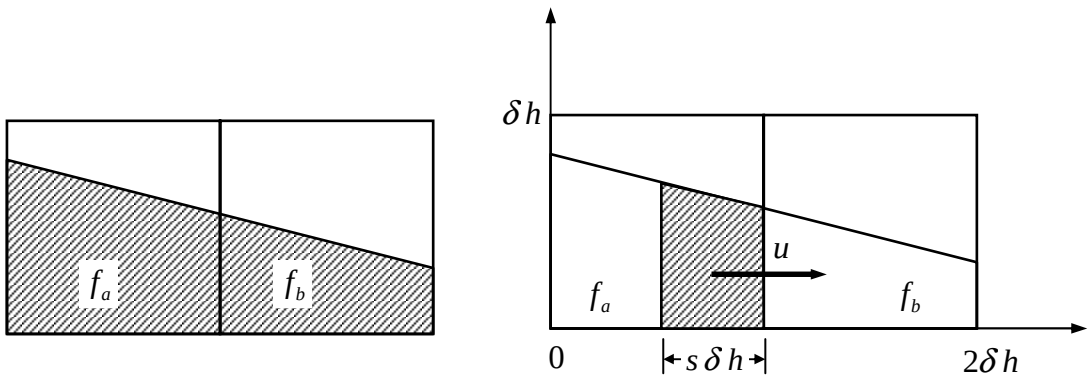


(a) Surface structure (b) flux of fluid in one time step

Figure 5. Example of fluid flux calculation in FLAIR method.

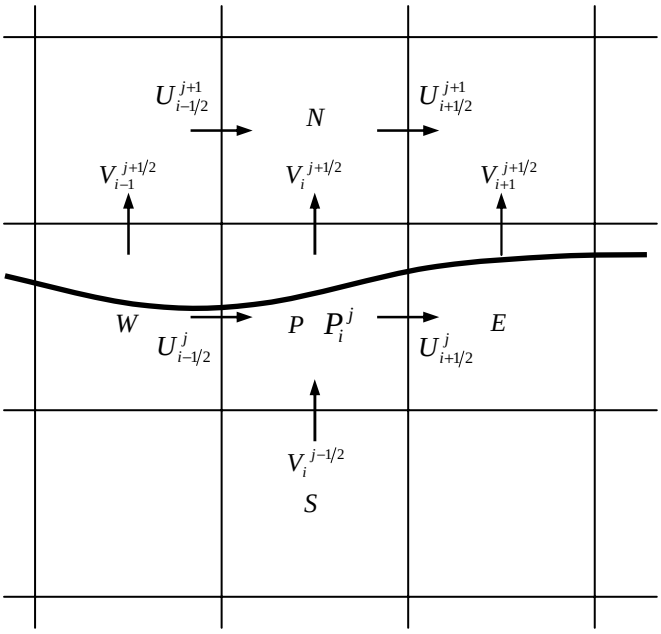


(a) Nearly horizontal surface

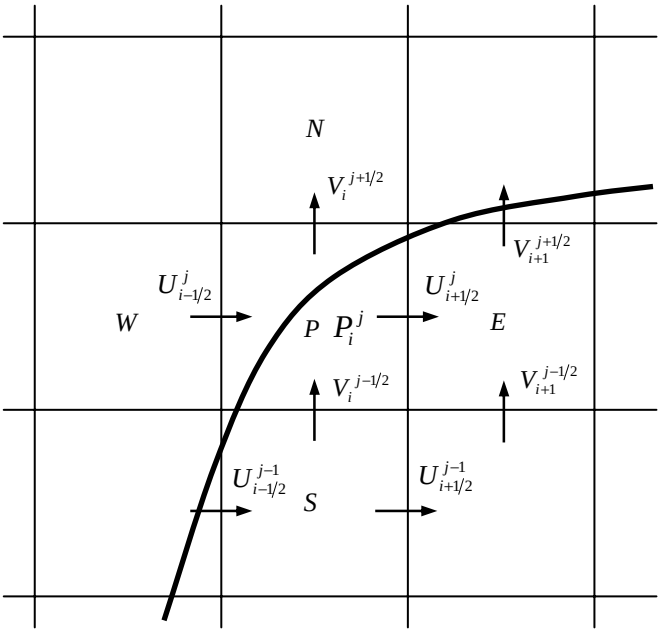


(b) Nearly 45° sloped surface

Figure 6. Velocity and pressure boundary conditions on free surface.

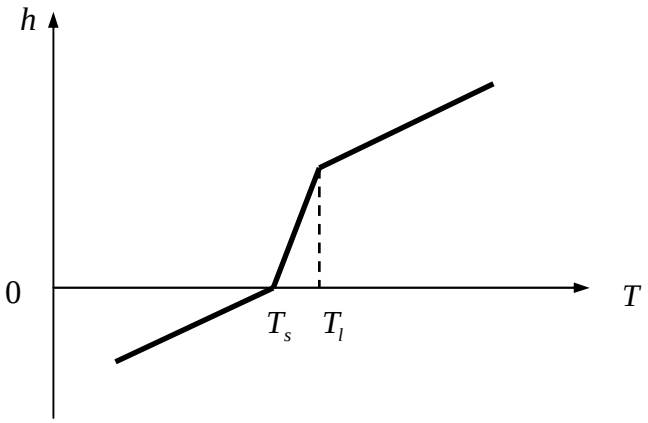


Figure 7. The enthalpy-temperature relation.

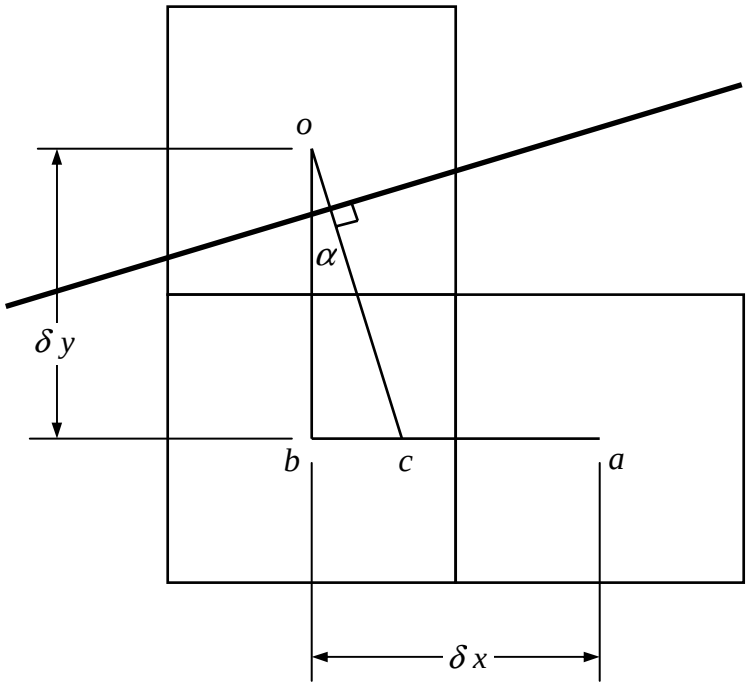


Figure 8. Applying Neumann boundary conditions on a surface cell.

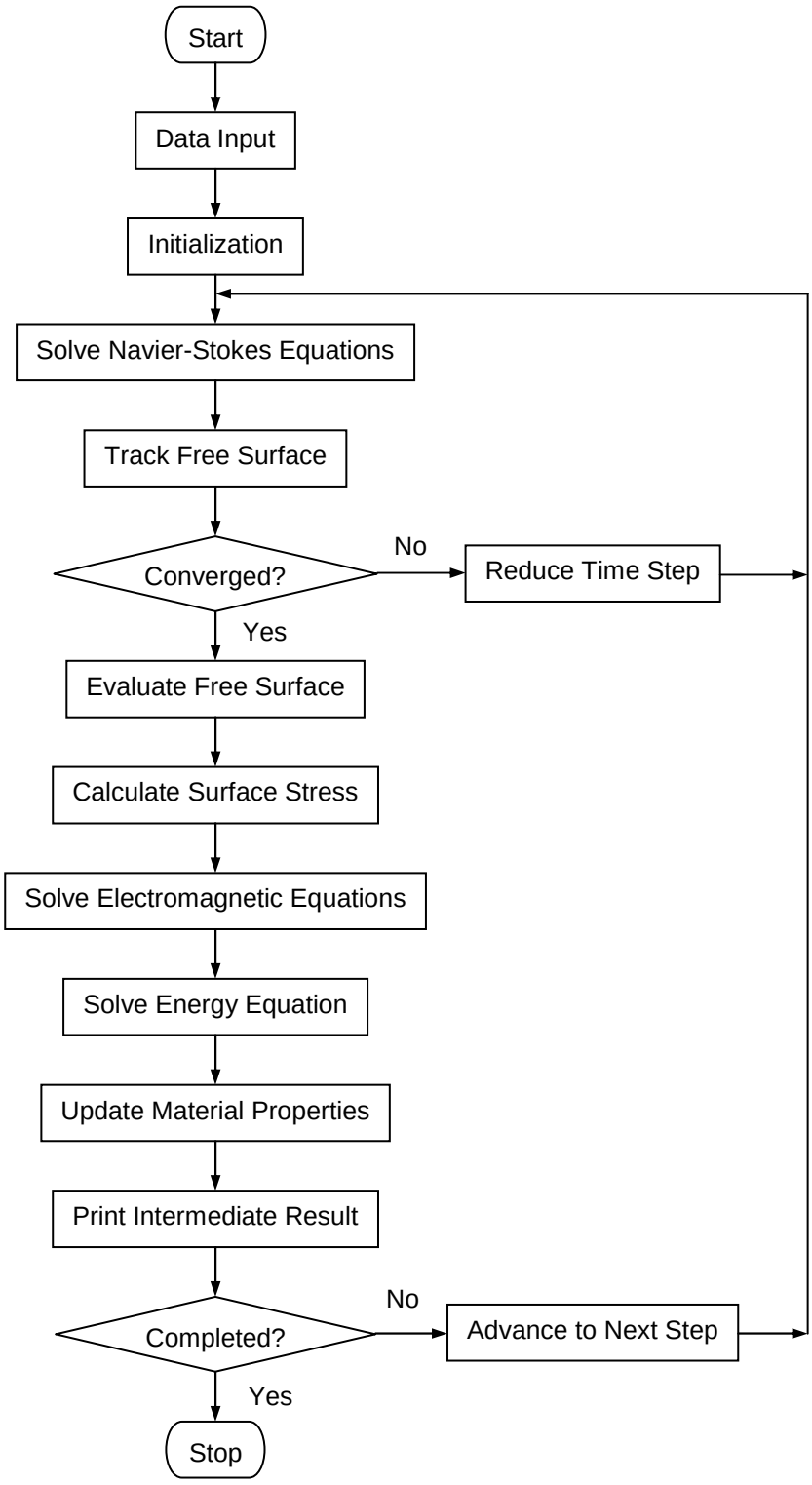


Figure 9. Flow chart of computational procedure.

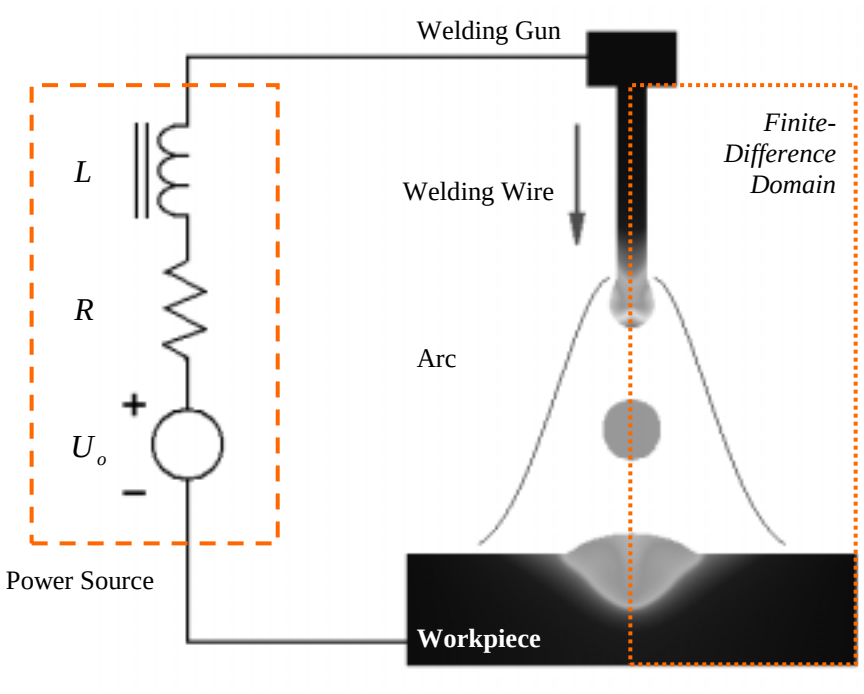


Figure 10. Axisymmetric modeling of gas metal arc welding.

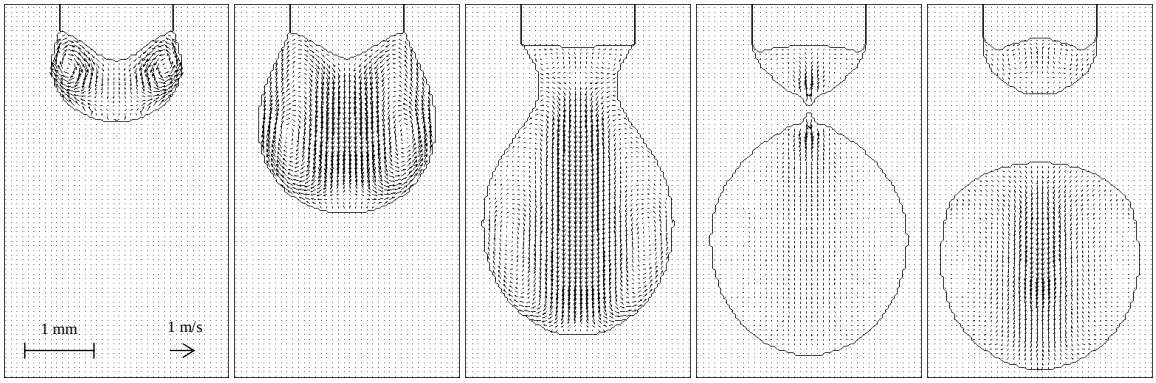


170 ms 260 ms 340 ms 342.75 ms 344 ms

(a) Globular Transfer (200A)

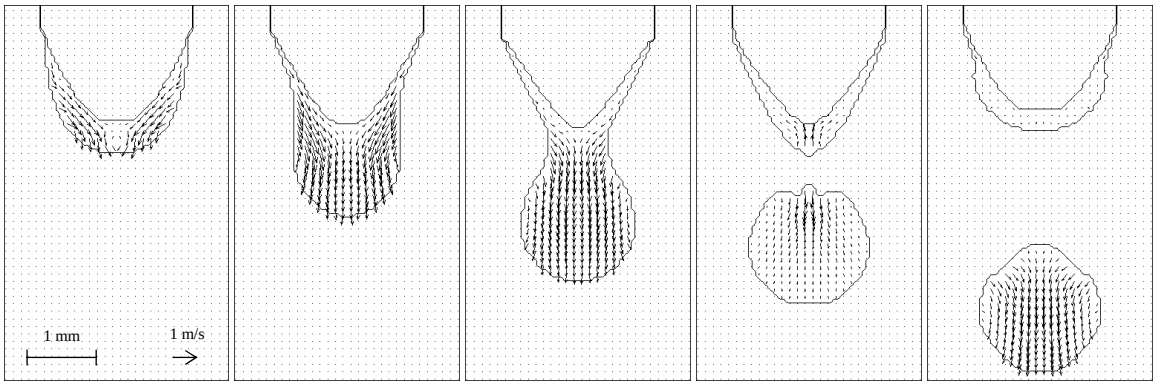


34.0 ms 35.5 ms 36.3 ms 36.5 ms 37.0 ms

(b) Spray Transfer (350A)

Figure 11. Simulated procedure of droplet detachment in gas metal arc welding.

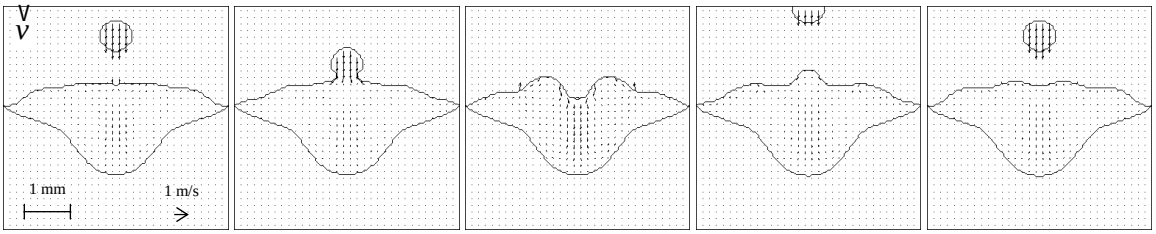


303.0 ms 304.0 ms 305.5 ms 307.0 ms 308.0 ms

(a) Velocity distribution

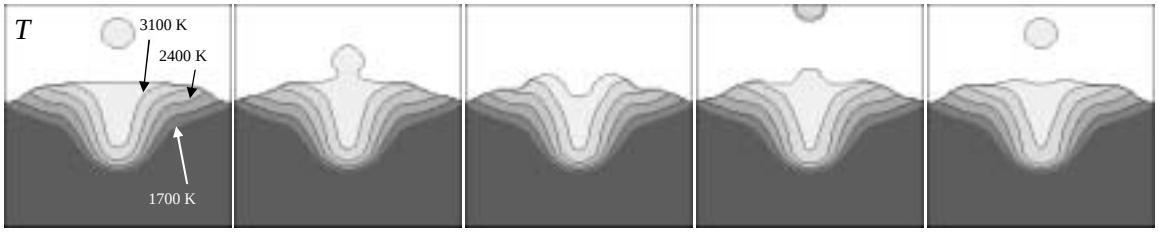


303.0 ms 304.0 ms 305.5 ms 307.0 ms 308.0 ms

(b) Temperature distribution

Figure 12. Simulated procedure of weld pool development in gas metal arc welding.

Table 1. Material properties of workpiece and welding wire

| Property | Symbol | Value | Unit | Reference |
|---|---|---|---|---|
| Density | $\rho$ | 7200 | $kg \cdot m^{-3}$ | [22] |
| Melting Temperature | $T_m$ | 1727 | $K$ | [22] |
| Latent Heat | $L$ | $2.47\times10^{5}$ | $J \cdot kg^{-1}$ | [22] |
| Specific Heat (solid) | $c_s$ | 700 | $J \cdot kg^{-1} \cdot K^{-1}$ | [22] |
| Specific Heat (liquid) | $c_l$ | 780 | $J \cdot kg^{-1} \cdot K^{-1}$ | [22] |
| Thermal Conductivity | $k_l$ | 22 | $W \cdot m^{-1} \cdot K^{-1}$ | [22] |
| Dynamic Viscosity | $\mu$ | 0.006 | $kg \cdot m^{-1} \cdot \sec^{-1}$ | [22] |
| Kinematic Viscosity | $\nu$ | $8.3\times10^{-7}$ | $m^2 \cdot \sec^{-1}$ | Calculated |
| Surface Tension Coefficient | $\gamma$ | 1.2 | $N \cdot m^{-1}$ | [14] |
| Electric Conductivity | $\sigma$ | $7.14\times10^{5}$ | $\Omega^{-1} \cdot m^{-1}$ | [22] |